

KMTNET NEARBY GALAXY SURVEY I. : OPTIMAL STRATEGY FOR LOW SURFACE BRIGHTNESS IMAGING WITH KMTNET

WOOWON BYUN^{1,2}, YUN-KYEONG SHEEN¹, LUIS C. HO^{3,4}, JOON HYEOP LEE^{1,2}, SANG CHUL KIM^{1,2}, HYUNJIN JEONG¹,
BYEONG-GON PARK^{1,2}, KWANG-IL SEON^{1,2}, YONGSEOK LEE^{1,5}, SANG-MOK CHA^{1,5}, MINJIN KIM^{1,2,6}

Draft version October 5, 2018

ABSTRACT

In hierarchical galaxy formation models, galaxies evolve through mergers and accretions. Tidally-disrupted debris from these processes can remain as diffuse, faint structures, which can provide useful insight into the assembly history of galaxies. To investigate the properties of the faint structures in outskirts of nearby galaxies, we conduct deep and wide-field imaging survey with KMTNet. We present our observing strategy and optimal data reduction process to recover the faint extended features in the imaging data of NGC 1291 taken with KMTNet. Through the dark sky flat-fielding and optimal sky subtraction, we can effectively remove inhomogeneous patterns. In the combined images, the peak-to-peak global sky gradients were reduced to less than $\sim 0.5\%$ and $\sim 0.3\%$ of the original B - and R -band sky levels, respectively. However, we find local spatial fluctuations in the background sky which can affect the precise measurement of the sky value. Consequently, we can reach the surface brightness of $\mu_{B,1\sigma} \sim 29.5$ and $\mu_{R,1\sigma} \sim 28.5$ mag arcsec⁻² in azimuthally averaged one-dimensional surface brightness profiles, that is mainly limited by the uncertainty in the sky determination. These results suggest that the deep imaging data produced by KMTNet are suitable to study the faint features of nearby galaxies such as outer disks and dwarf companions, but unideal (not impossible) to detect stellar halos. The one-dimensional profile revealed that NGC 1291 appeared to have Type I disk out to $R \sim 30$ kpc with no obvious color gradient and excess light due to a stellar halo was undetected.

Keywords: galaxies: individual (NGC 1291) – galaxies: stellar content – galaxies: structure – galaxies: optical

1. INTRODUCTION

In the Λ CDM model, galaxies grow their masses through mergers and accretions (White & Rees 1978). These processes can leave the disturbed structures in the outskirts of galaxies which are remnants of tidally-disrupted satellite galaxies (Bullock et al. 2001; Bullock & Johnston 2005; Johnston et al. 2008; Cooper et al. 2010). While distinct structures such as shells, tails, and stellar streams remain from recent or ongoing merger events ($t_{\text{lookback}} \sim 4-5$ Gyr), more ancient mergers form well-mixed stellar halos which have extremely low surface brightness (cf. De Lucia & Helmi 2008; Johnston et al. 2008; Morales et al. 2018). Therefore, the presence and properties of the merging features in the galaxy outskirts provide direct hints about the recent mass assembly histories of galaxies (e.g., Bullock et al. 2001; De Lucia & Helmi 2008; Johnston et al. 2008).

However, there have not been many studies to observe these signatures because of their low surface brightness, followed by expensive observational costs. It is generally required to reach a surface brightness of $\sim 27-28$ mag arcsec⁻² to detect tidal debris and stellar halos (Courteau et al. 2011; Bakos & Trujillo 2012). Nevertheless, there have been several studies which show the presence of post-merger signatures in nearby galaxies. For example, Malin (1979) and

Schweizer (1980) revealed the existence of shells or loops in elliptical galaxies. Then Schweizer & Seitzer (1988) showed the presence of shell features in disk galaxies at a distance within ~ 100 Mpc, suggesting that merging features are not exclusive to elliptical galaxies. Furthermore, similar searches for merging features have been conducted for nearby galaxies (e.g., Tal et al. 2009; Martínez-Delgado et al. 2010; Duc et al. 2015; Watkins et al. 2015; Mihos et al. 2017) and more distant ones (e.g., van Dokkum 2005; Sheen et al. 2012; Atkinson et al. 2013).

Recently, there have been several attempts to explore the properties of merging features and stellar halos in the outskirts of very nearby galaxies using the integrated light of galaxies (e.g., Mihos et al. 2013; van Dokkum et al. 2014; Merritt et al. 2016; Trujillo & Fliri 2016; Watkins et al. 2016), which requires not only deep imaging, but also wide fields-of-view (FoV) detector. This method can be applicable to relatively distant galaxies and thus larger sample, compared to one of the optimal method using the resolved star counts in the stellar halos with Hubble Space Telescope (e.g., GHOSTS survey; Radburn-Smith et al. 2011; Harmsen et al. 2017). However, it is technically challenging to investigate photometric properties of the galaxy outskirts due to its diffuse structures with extremely low surface brightness. Therefore, it requires not only dedicated data reduction to recover the faint extended starlight from stellar halos, but also careful data analysis to quantify its physical properties. Despite these difficulties, they could detect merging features and stellar halos with surface brightness deeper than ~ 28 mag arcsec⁻² and estimated their masses and colors. Previous studies (van Dokkum et al. 2014; Merritt et al. 2016; Trujillo & Fliri 2016) have shown that the mass fraction of stellar halos substantially varies with a large scatter, but is in broad agreement with the predictions from the numer-

¹ Korea Astronomy and Space Science Institute, Daejeon 34055, Korea

² Korea University of Science and Technology, Daejeon 34113, Korea

³ Kavli Institute for Astronomy and Astrophysics, Peking University, Beijing 100871, China

⁴ Department of Astronomy, School of Physics, Peking University, Beijing 100871, China

⁵ School of Space Research, Kyung Hee University, Yongin, Kyeonggi 17104, Korea

⁶ Department of Astronomy and Atmospheric Sciences, Kyungpook National University, Daegu 702-701, Korea

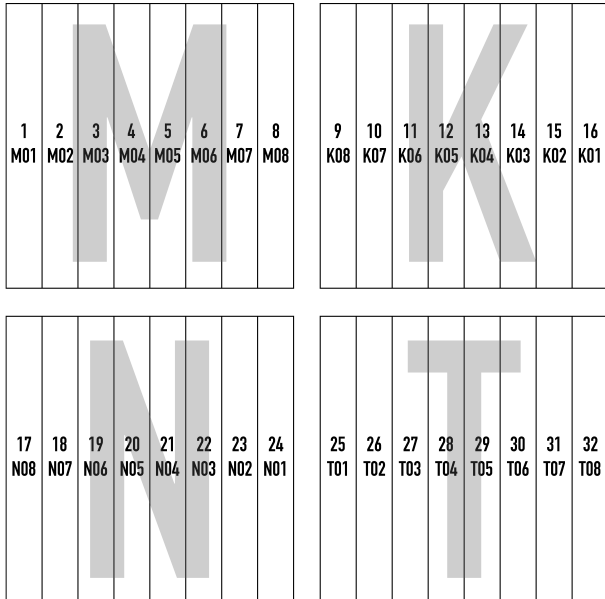


Figure 1. The configuration of the KMTNet mosaic CCD imager. It consists of four $9k \times 9k$ CCD chips (M, K, N, and T), each of which employs eight amplifiers. The gap between CCDs is ~ 184 arcsec in the horizontal direction and ~ 373 arcsec in the vertical direction. The order and name of each amplifier are also indicated.

cal simulations (e.g., Cooper et al. 2010; Pillepich et al. 2014; Harmsen et al. 2017). It reveals that the mass assembly history of galaxies might differ despite having similar total stellar masses.

In the same manner, we are conducting a deep imaging survey of nearby galaxies in the southern hemisphere with Korea Microlensing Telescope Network (KMTNet; Kim et al. 2016). KMTNet consists of three 1.6-m identical telescopes in three different sites (Cerro-Tololo in Chile, Sutherland in South Africa, and Siding Spring Observatory in Australia). Each telescope contains an imaging camera with a $2^\circ \times 2^\circ$ of FoV to monitor stars in Galactic bulge in order to search for the microlensing events.

Although KMTNet has wide FoV of detectors, it is not originally developed for detecting low surface brightness features. Therefore, an optimized observing strategy and data analysis with a great precision are required in order to discriminate the diffuse light in the galaxy outskirts from the scattered light, residuals of sky background and contamination from Galactic cirrus. To achieve the precision to reach a surface brightness of $\sim 27-28$ mag arcsec $^{-2}$, it is necessary to minimize the sky variation up to 0.5% of the sky level through rigorous flat-fielding and sky subtraction. In that respect, the wide FoV of KMTNet detector enables us not only to determine sky values and global sky gradients precisely, but also to construct a dark sky flat with blank fields. However, no such attempts have yet been made in other KMTNet projects (Kim et al. 2016). This experiment was the first attempt to overcome the difficulties caused by using sub-optimal systems for detecting integrated diffuse light in nearby galaxies. In this paper, we present observing strategy and optimal data reduction method to recover the extended faint structures using KMTNet data and describe initial results of our survey. Section 2 provides an overview of the observation strategy and targets. Section 3 describes the basic data reduction methods. Section 4 presents the sky

Table 1
Basic properties of NGC 1291

Properties	Value
Classification	(R)SB0/a(s)
Inclination	12°
R.A. (J2000)	$03^h 17^m 18^s .6$
Decl. (J2000)	$-41^\circ 06' 29''$
Distance	10.1 Mpc
m_B	9.44 mag

determination method with imaging data of NGC 1291 and the radial profile of the galaxy to show how deep the survey data can reach, as a pilot study. We summarize our results in Section 5.

2. OBSERVATIONS OF NGC 1291

A deep optical imaging survey of nearby galaxies was being conducted by taking advantage of the wide FoV ($2^\circ \times 2^\circ$) of the three KMTNet 1.6-m telescopes. The KMTNet imager consisted of four $9k \times 9k$ CCD chips (M, K, N, and T), each of which employed eight amplifiers, as illustrated in Figure 1. The pixel scale is 0.4 arcsec and the gap between CCDs is ~ 184 arcsec in the horizontal direction and ~ 373 arcsec in the vertical direction. The exposure time of each object frame is 120 seconds. Object frames were obtained by placing a target galaxy at the center of each chip to secure large sky areas for dark sky flat-fielding around a galaxy. Then the images were taken following the 7-points dithering in each chip to fill the gap between four of the chips. As a result, the final stacked image would have a $3^\circ \times 3^\circ$ FoV around the target galaxy. We obtained images of target galaxies for the same band using a single telescope at Cerro-Tololo to avoid troubles from different characteristics between three telescopes and keep consistency of dataset.

Our targets are originally selected from the catalog of Carnegie-Irvine Galaxy Survey (CGS; Ho et al. 2011), which conducted an imaging survey of nearby galaxies with $B_T \leq 12.9$ mag in the southern hemisphere. As a pilot study, we chose NGC 1291 which has a largest angular size among our sample, and also has a negligible contamination of Galactic cirrus. Therefore, this target is appropriate to test whether we can reach the precision required to study faint outskirts of nearby galaxies with KMTNet. Some basic properties of NGC 1291 are listed in Table 1. The data of NGC 1291 analyzed in this study were taken at KMTNet-CTIO observatory on November 12, 2015. During the night, the weather was clear and the average seeing was about 1.1 arcsec.

3. DATA PROCESSING

3.1. Overscan correction

Prior to data reduction, we performed visual inspection of the dataset in order to discard images with artifacts due to mis-tracking of the telescope or abnormal jump of bias level in a part of detectors. Consequently, 85 *B*-band and 48 *R*-band images of NGC 1291 were utilized in the study, corresponds to the total exposure time of ~ 2.8 and ~ 1.6 hrs, respectively. We initially reduced the raw data using IRAF's `mscred` package to process MEF (Multiple Extension FITS) files of the KMTNet.

First, overscan correction and image trimming were performed on all object and calibration frames. In general, it would be followed by bias correction with a master bias

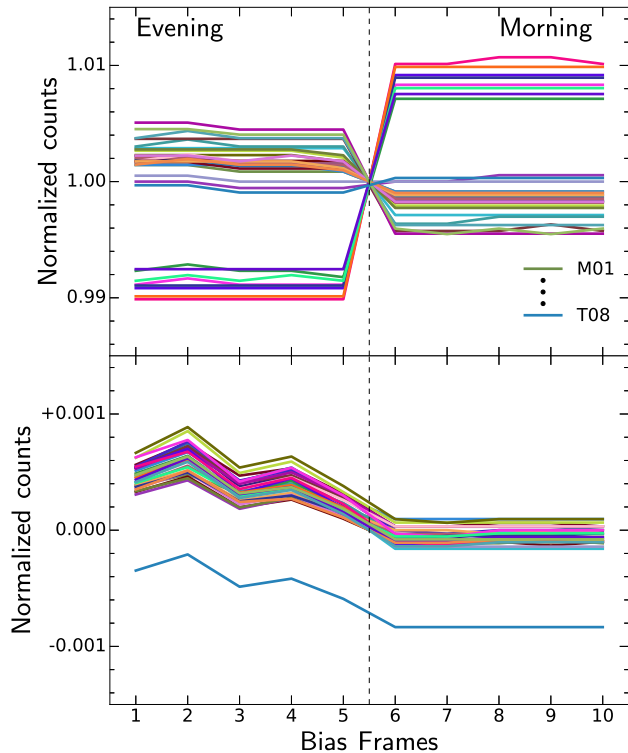


Figure 2. *Top:* Variations of bias level in each amplifier along the 10 bias frames taken in the evening and the morning of the observing run. Different colors represent different amplifiers. Counts are normalized to the median bias level of all amplifiers of 10 bias frames. Not only the bias levels significantly change during the night up to $\pm 1\%$, but also their patterns are inconsistent with each other. *Bottom:* Same as the top panel, but after overscan correction is conducted. Although variations in bias level still remain, the amplitudes of the variations are negligible relative to the original bias level ($< 0.1\%$). Note that ‘T08’ is unlike other amplifiers, but its residual is still less than $\sim 0.1\%$.

frame. However, we found that the bias levels had significantly varied for 10 bias frames which were taken at the beginning and end of the observation. In order to check the degree of variations in the bias level, we compared relative median counts of amplifiers along the different bias frames, as shown in the upper panel of Figure 2. It demonstrates that the bias levels varied up to 1% in each amplifier during the night. Therefore, we decided not to conduct bias correction to the images because a master bias frame would not accurately represent the bias level of the data.

According to our experiments, the bias levels could be corrected suitably when their own overscan regions were utilized. As shown in the bottom panel of Figure 2, we found that the bias levels were reduced to almost zero counts after overscan correction. Note that the original bias level is $\sim 1,700$ counts on average. Although there some offsets remained, they were less than 0.1% of the original bias level, so their effect was negligible. The standard deviation of each bias frame was reduced to ~ 0.26 counts, which is much smaller than the sky variation aimed for our deep imaging survey. From these results, we could assume that overscan is nearly synchronized with varying bias levels. Therefore, we adopted overscan correction as a standard procedure for bias subtraction of the KMTNet data. Dark correction was not applied either because dark counts were negligible to be almost zero.

3.2. Dark sky flat-fielding

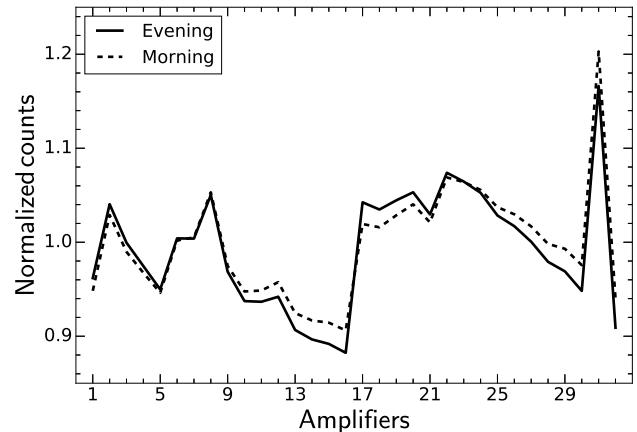


Figure 3. The normalized counts of the twilight flats in R -band as a function of 32 amplifiers. The median value in each frame is normalized to the median of the all amplifiers in the same frame. Solid and dashed lines represent two twilight flats observed in the evening and morning, respectively. Due to the intrinsic sky gradient varying over time, the patterns between two twilight flats appear to change by up to $\sim 5\%$ of the sky level. Note that twilight flats in B -band exhibit the similar pattern.

KMTNet observatories did not provide dome flats in 2015, so we attempted flat-field correction using twilight flats first. However, it turned out that it is almost impossible to keep a consistent illumination pattern between twilight flats over the large sky area of $2^\circ \times 2^\circ$ FoV. Figure 3 shows a comparison of twilight flats taken in the evening (solid line) and the morning (dashed line). The median counts for each amplifier were normalized by the median of all amplifiers in the same frame. We found that the illumination patterns of two twilight flats did not match, probably due to the combined effects of the intrinsic sky gradient varying over time and the wide FoV of the KMTNet CCDs.

Instead, we conducted dark sky flat-fielding for object frames. Dark sky flats were generated by stacking all object frames in each band. Prior to the stacking, all astronomical sources in the overscan-corrected object frames were masked using `objmasks` in IRAF. The objects were initially identified as being 1.4σ above the sky value. In addition, diffuse light near the target galaxy and artifacts around bright stars were manually masked out. The `photutils` library in the PYTHON package was used to find the position and relative intensity of bright sources. The size of mask is enlarged according to the brightness of each masked source. In total, 85 B -band images and 48 R -band images were combined for each band using `sflatcombine` in IRAF to generate the master flat.

Figure 4 shows the object frames after twilight flat-fielding (left) and dark sky flat-fielding (right). We found that dark sky flat-fielding effectively removes inhomogeneous illumination patterns in object frames. The background variation among amplifiers was sufficiently eliminated and only intrinsic sky gradient remained across the image.

3.3. Sky subtraction and Image combining

We used the dark sky flat to generate the bad pixel mask that contains bad pixels, bad columns, and hot pixels. Those pixels were replaced by linearly interpolating the nearest pixels.

After dark sky flat-fielding, there was still an intrinsic sky gradient arising from the combination of sky background distorted by zenith distance and the wide FoV of the KMTNet data as shown in the right image of Figure 4. We found that

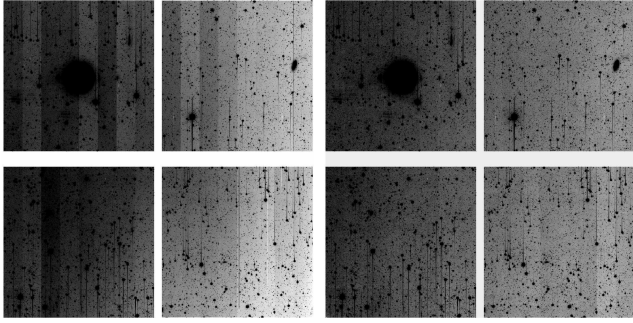


Figure 4. The object frames after twilight flat-fielding (left) and dark sky flat-fielding (right). This difference demonstrates that dark sky flat-fielding effectively corrects different background levels between amplifiers, creating a smooth background gradient better than twilight flat-fielding.

the shape and amplitude of the sky gradient varied significantly during the night. Peak-to-peak variation of the sky gradients varied up to $\sim 3\%$ of the median sky value in both bands. Note that the peak-to-peak variation was defined as the fractional difference between the minimum and maximum sky values measured in each amplifier. This variation in sky gradients may have created global fluctuations in the backgrounds of stacked images, affecting the measurements of surface brightness radial profiles of target galaxies.

In order to remove the sky gradient from individual object images, we performed modeling of the two-dimensional sky in each object frame and subtracted the sky model from the image. First, we merged 32 amplifiers in each object frame into a single extension image. Then we binned each object frame by $\sim 500 \times 500$ pixels, which is suitable for discarding unmasked hot pixels and smoothing over any peculiar features in the background. Then a two-dimensional polynomial fit with a second order for a sky background was conducted⁷. Figure 5 shows an example of the original sky gradient with object masks (left) and the sky model (middle) in the binned image. The blanked region shown in the left panel was not used for the polynomial fitting. It appears that the sky model with a two-dimensional polynomial fit worked reasonably well. The right panel of Figure 5 shows the sky-subtracted image using the two-dimensional sky model. The peak-to-peak variation was reduced to less than $\sim 1.65\%$ and $\sim 0.65\%$ of the original sky levels in *B*- and *R*- bands, respectively.

Before combining all object images into a mosaic image in each band, astrometric calibration was conducted following the instruction of ‘‘Astrometric calibration for KMTNet data’’, provided by the KMTNet project team⁸. The brief description of the process is as follows. 1) We merged the amplifiers into four separate chips. 2) Using the coordinates of astronomical sources from each chip, we separately derived the astrometric solution using *SCAMP* (Bertin 2006). 3) The final astrometric solutions were applied to the sky-subtracted images. At last, the final mosaic images were generated using *Swarp* (Bertin et al. 2002).

3.4. Standardization

Photometric zero points for the combined images were determined using bright stars in the field of NGC 1291. We per-

⁷ The polynomial fits with higher orders do not appear to be superior to the second order fit. Thus, we decided to adopt the second order fit in order to avoid removing the intrinsic faint features of the target galaxy during the sky subtraction (see also Feldmeier et al. 2004).

⁸ <http://kmtnet.kasi.re.kr>

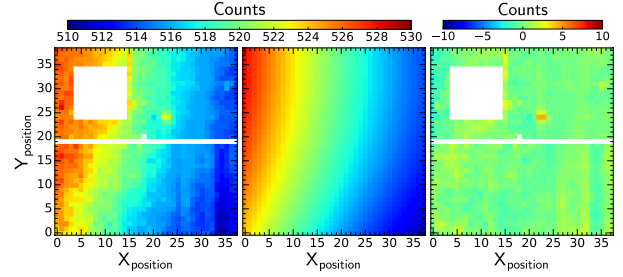


Figure 5. *Left:* The intrinsic sky gradient of the right image in Figure 4, binned by $\sim 500 \times 500$ pixels. The target galaxy and the gap between chips are blanked. *Middle:* The sky value modeled by a two-dimensional polynomial fit with a second order. *Right:* The sky-subtracted image. The global pattern of the intrinsic sky gradient appears to be successfully subtracted. The color represents the count of each pixel and the scale is shown on the upper side.

formed aperture photometry of the stars for the combined images using *SExtractor* (Bertin & Arnouts 1996) and compared them with the magnitudes in the catalog of AAVSO Photometric All-Sky Survey (APASS) DR9⁹. We chose the radius of aperture of 10 arcsec which is matched for that of APASS catalog. Note that APASS catalog provides the magnitudes of *B*, *V*, *g'*, *r'*, *i'* bands. Therefore, we converted *g'* and *r'* magnitudes in APASS catalog to *R* magnitude, using the conversion equation $R = r - 0.1837(g - r) - 0.0971$ provided by Lupton (2005).

Figure 6 shows the comparison between the APASS magnitudes of stars and their total counts from the KMTNet images measured within the aperture of $r = 10$ arcsec. We excluded saturated stars and ones in the crowded regions for the fit. The standardization equation for the combined images is as follows.

$$m_* = -2.5 \log(\text{count}) + m_{*,0} \quad (* : B \text{ or } R) \quad (1)$$

The fit showed that the photometric zero points were determined to be $m_{B,0} \sim 29.39 \pm 0.08$ and $m_{R,0} \sim 29.52 \pm 0.06$.

4. ASSESSMENT: RADIAL PROFILE OF NGC 1291

In order to assess our deep optical images obtained with KMTNet, we derived surface brightness radial profiles of NGC 1291 using the combined images. First, we masked out all of the astronomical sources and then ascertained the sky level which should have been zero due to the optimal sky subtraction (§3.3). As shown in Figure 7, the medians of the sky level in the combined mosaic images are close to zero in both bands, and the $1-\sigma$ variations of the sky backgrounds are 0.8 DN/pixel and 2.1 DN/pixel in *B* and *R* bands, respectively. Therefore, the $1-\sigma$ depths of surface brightness calculated based on the standard deviations are ~ 28.7 and 27.7 mag arcsec⁻² in *B*- and *R*-bands, respectively. Distributions of sky values appears to follow Gaussian profile, revealing that the background is uniform and the astronomical sources are properly masked out. Recently, Park et al. (2017) reported newly discovered dwarf galaxies in NGC 2784 group using deep images obtained with KMTNet telescopes. The $1-\sigma$ depths of surface brightness of their images are $\mu_B \sim 28.3$, $\mu_V \sim 27.6$, $\mu_I \sim 27.3$ mag arcsec⁻², which are comparable with our results. It suggests that our data can be used to search dwarf galaxies around NGC 1291.

⁹ <https://www.aavso.org/apass>

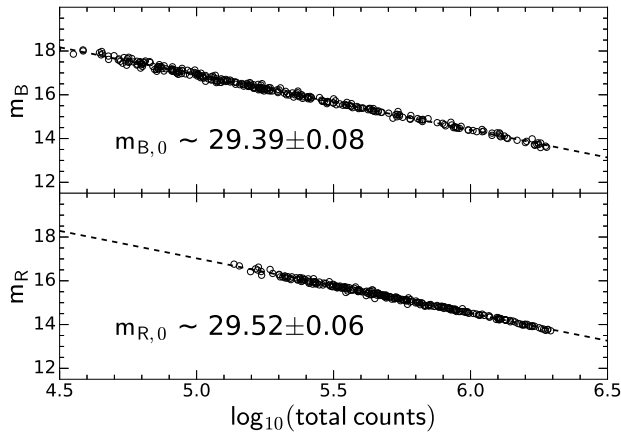


Figure 6. The APASS magnitudes of the stars (circles) as a function of their total counts within an aperture ($r = 10$ arcsec) in the combined images. Saturated stars and stars in the crowded regions were excluded from the fit. The results show tight correlations (dashed lines) between the magnitudes given by APASS and total counts measured in the images.

On the other hand, the $1\text{-}\sigma$ depth in the azimuthally averaged one-dimensional profile can be significantly larger (fainter) than the values derived from the standard deviation of the sky background. The overall uncertainty of mean surface brightness in each isophote can be reduced by \sqrt{N} through the azimuthal average where N is the number of pixels in the isophote. Because the target galaxy has a large apparent size, there can be a substantial number of pixels on each isophote in one-dimensional fit. Therefore, if the sky background is uniform, we could reach deeper surface brightness in one-dimensional profile (see also Mihos et al. 2013; Merritt et al. 2016).

4.1. Sky determination

Accurate sky determination is crucial to derive one-dimensional light profile precisely because the surface brightness of the outskirts of target galaxies is at least 50–100 times fainter than the sky brightness. Although we carefully subtracted the sky value in the individual object frames, there can still remain residuals in the sky background. We found that the combined mosaic images exhibit a local spatial fluctuation around the target galaxy. The right panel of Figure 8 shows the distribution of sky levels in the vicinity of NGC 1291 in a 500×500 pixel-binned R -band image. The color represents the median count in each binned pixel. This sky fluctuation can introduce an uncertainty in the sky level measurement, which in turn can introduce additional error budget in the light profile. Sky fluctuations can be caused by imperfect masking of bright sources, and/or underlying Galactic cirrus, but neither can be regarded as the origin of the fluctuation. We found that the astronomical sources are properly masked from the distribution of the sky background and the sky fluctuation appears not to be coincident with nearby bright sources. From the IRAS map, we found $F_{100\mu\text{m}} \sim 1.5 \text{ MJy sr}^{-1}$ in the vicinity of NGC 1291, revealing the contribution from the Galactic cirrus is negligible (cf. Merritt et al. 2016). While it is unclear what the origin of the sky fluctuation is, we chose to take an uncertainty in the sky determination into account when we investigate the surface brightness profile of NGC 1291.

To measure the sky level in the final mosaic image, we adopt four different regions. As shown in the left panel of Figure 8, we estimated sky values from different annuli along

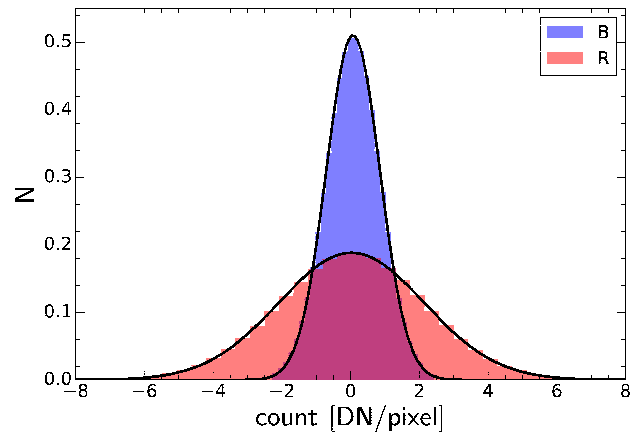


Figure 7. The normalized histograms of the pixel values of sky background for combined images. Blue and red histograms represent B - and R -bands, respectively. Black lines show the fit with the Gaussian function. Their peak positions are 0.07 and 0.02 DN/pixel and their standard deviations are 0.8 and 2.1 DN/pixel in B - and R -bands, respectively.

the distance from the galaxy center. Mihos et al. (2013) presented that the starlight can be detected up to nearly $3 \times R_{25}$ in the deep images of M101. We conservatively chose the annulus for the sky determination beyond ~ 20 arcmin, which is approximately equivalent to $4 \times R_{25}$ of NGC 1291 (cf. $D_{25} = 9.8$ arcmin; de Vaucouleurs 1975). The width of each sky region was set to ~ 3.5 arcmin. We found that the sky value varies between 0.02 (0.09) and -0.16 (0.06) for $R(B)$ band image, seemingly due to local sky fluctuations. Although these variations are less than $\sim 0.05\%$ of the original sky values, they can induce significant errors in surface brightness profiles, especially in the faint regions. In other words, our investigation for a deep imaging is mainly limited by local sky fluctuations, rather than $1\text{-}\sigma$ variations in the sky background. Once the sky level was estimated, we subtracted the sky value from the mosaic image.

4.2. Surface brightness profiles of NGC 1291

As shown in Figure 9, stellar light can be detected up to ~ 10 arcmin in the two-dimensional image, which corresponds to $R \sim 30$ kpc. In order to investigate the capability of KMTNet for a deep imaging survey, we derived the one-dimensional surface brightness profile of NGC 1291 using the `ellipse` task in IRAF. When conducting the isophotal fit, we fixed the central position but other parameters were allowed to be fit as free parameters. As we discussed in §4.1, there was an uncertainty in the background level up to 0.05% of the original sky values. In order to account for this uncertainty, we estimated the surface brightness profiles by varying sky levels as described in §4.1. The best surface brightness profile was determined by employing the median value at a given radius. The scatter in the surface brightness profiles was implemented to compute the uncertainty. Note that the overall uncertainty in the outskirts was dominated by the scatter due to the uncertainty in the background level rather than the variance within the isophote.

Figure 10 shows the surface brightness profile of NGC 1291 in B - and R -bands. The $1\text{-}\sigma$ depths of surface brightness in one-dimensional profiles are ~ 29.5 and $28.5 \text{ mag arcsec}^{-2}$ in B - and R -bands, respectively. The vertically shaded area in Figure 10 denotes the inner radius ($5 \times R_h$; 20–25 kpc) where the light from the stellar halo is expected to dominate the total stellar light (Merritt et al. 2016). Theoretical and observa-

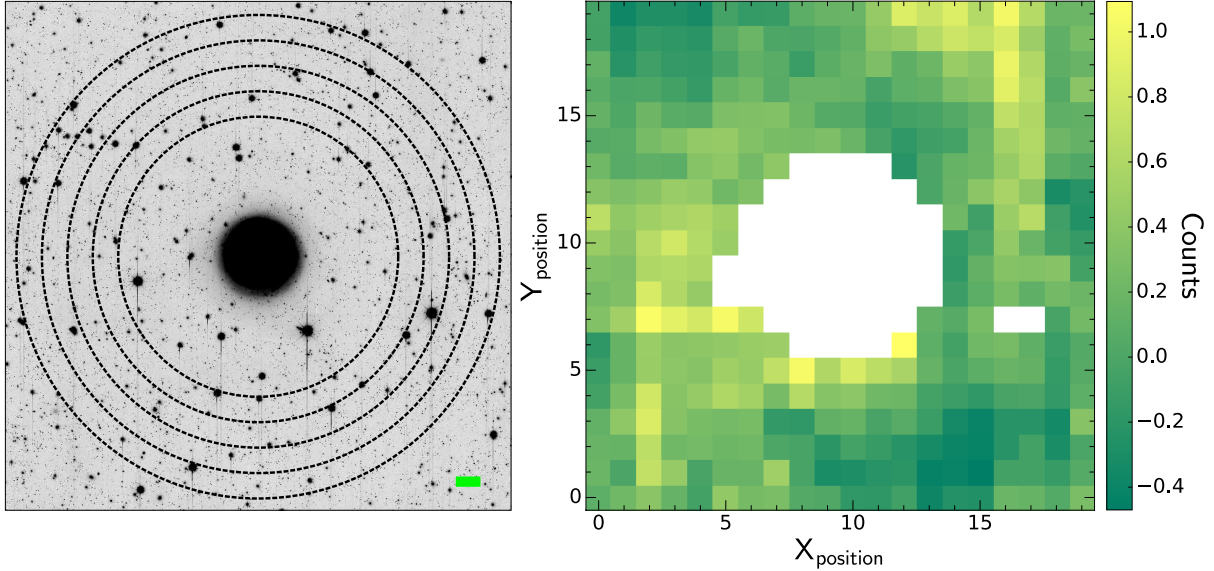


Figure 8. *Left:* Four different regions used for sky determination are denoted as dashed lines. They are 20–30 arcmin from the center of NGC 1291, and the width of the each region is 3.5 arcmin. The green horizontal bar indicates the scale of 3.5 arcmin (~ 10 kpc). *Right:* The distribution of sky levels in the 500×500 pixel-binned R -band image. The color represents the count of each pixel and the scale is shown on the right side. The FoV of the two panels is $\sim 1^\circ \times 1^\circ$.

tional studies of the Milky Way Galaxy have also suggested that stellar light is dominated by the halo rather than the disk component beyond a radius of ~ 20 kpc (Carollo et al. 2010; Pillepich et al. 2014). This is consistent with the fact that NGC 1291 and the Milky Way Galaxy have similar physical properties in terms of stellar mass ($M_{*,\text{NGC1291}} \sim 8 \times 10^{10} M_\odot$; Li et al. 2011, $M_{*,\text{MW}} \sim 4 - 5 \times 10^{10} M_\odot$; Bovy & Rix 2013) and half-light radius ($R_{h,\text{NGC1291}} \sim 4 - 5$ kpc, $R_{h,\text{MW}} \sim 2.74$ kpc; van den Bergh 2010). It reveals that our deep images obtained with KMTNet are deep enough to detect relatively bright features such as tidal streams, outer disks and dwarf companions (cf. Martínez-Delgado et al. 2010), but it might be challenging but not impossible to detect diffuse stellar halos at the outskirts of galaxies (Johnston et al. 2008; Courteau et al. 2011; Bakos & Trujillo 2012). For this reason, our ongoing survey will focus on the target of extended UV-disk (XUV-disk) galaxies which tend to have brighter and more discrete features at the outskirts than diffuse stellar halos (Thilker et al. 2007).

Although investigating the detailed structural properties is beyond the scope of this study, we briefly describe characteristics of the surface brightness profile of NGC 1291. NGC 1291 is known as a barred galaxy with an outer ring with a radius of ~ 9 kpc. The outer ring is more prominent in both UV and FIR images than in optical images, suggesting that a significant number of young stars and amount dust reside in the ring (Hinz et al. 2012). The feature of the outer ring can be clearly seen in the one-dimensional profile in Figure 10 (black arrow). While the color of the profile appears to be approximately constant in 2–25 kpc, $B-R$ color is the smallest (bluest) around the region of the ring, which is consistent with previous studies. The disk in spiral galaxies can be classified as three different groups depending on the shape of the disk profile: pure exponential profile (Type I); truncation profile (Type II); and anti-truncated profile (Type III); (Pohlen & Trujillo 2006). Applying the imaging decomposition for 1-D profile of NGC 1291, we found that the disk is

well described by a single exponential profile, indicating that NGC 1291 has Type I disk. The lack of dramatic variation in $B-R$ color is also consistent with color profile of Type I disk (Bakos et al. 2008).

One of the ultimate goals for this survey is to explore the halo structures using deep KMTNet images. Merritt et al. (2016) suggested that the halo features can be prominent at a radius above $5 \times R_h$, which is equivalent to 20–25 kpc for NGC 1291. Figure 10 shows that the light profile beyond 20–25 kpc does not deviate from the extrapolation of the exponential profile derived from the inner part of $R < 25$ kpc. It reveals that the halo contribution above a surface brightness of $28 - 29$ mag arcsec $^{-2}$ is insignificant in NGC 1291. Note that one would expect a few percent of stellar halo fractions at this mass (e.g., Courteau et al. 2011; van Vledder et al. 2016). This finding is in broad agreement with the results of Merritt et al. (2016), in the sense that spiral galaxies have a wide range of stellar halo mass fractions.

5. SUMMARY

We are carrying out a deep wide-field imaging survey of nearby galaxies in the southern hemisphere using KMTNet. The aim of this survey is to investigate the faint and extended structures of galaxies which contains the mass assembly histories of galaxies. In this study, we assess if imaging dataset of KMTNet is suitable to achieve our goal. We describe the detailed data reduction process using images of NGC 1291, one of the largest of the target galaxies. The data reduction was conducted as follows.

- The bias level appeared to vary up to $\pm 1\%$ over time, so we adopt overscan correction instead of using the master bias for the bias correction. The uncertainty due to the variation of the bias level was significantly reduced below $\sim 0.015\%$ to the original bias level.
- The twilight flat frames of KMTNet were severely affected by the intrinsic sky gradient owing to their wide

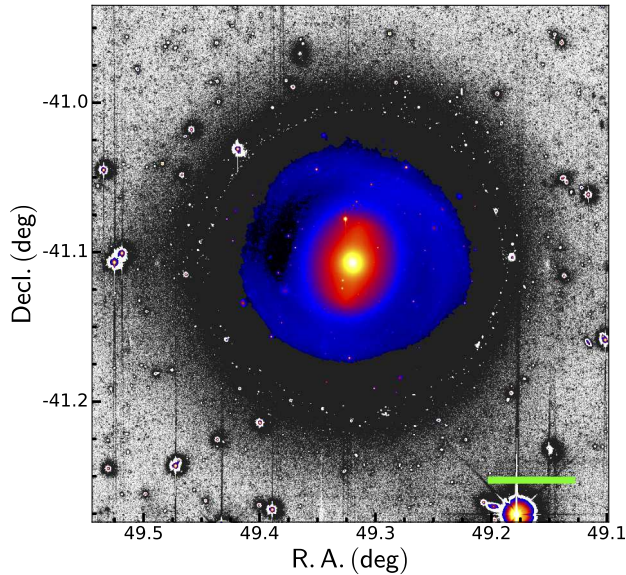


Figure 9. The combined R -band mosaic image of NGC 1291. While the faint extended region is shown in grayscale, the central part with the brighter surface brightness level is color-coded. The green horizontal bar indicates the scale of 10 kpc at a distance of 10.1 Mpc.

FoV. Therefore, the twilight flats appeared to be inappropriate for flat-field correction. Instead, we generated the dark sky flat using the object frames for flat-fielding. After flat-field correction with the dark sky flat, a peak-to-peak variation among amplifiers can be reduced up to $\sim 3\%$ of the original sky levels, which originated in the intrinsic sky gradient in the object frames.

- To remove the intrinsic sky gradient of the object frames, we employed a two-dimensional polynomial function with a second order to model the sky background, which is subtracted from the object frames. In so doing, the peak-to-peak variation among amplifiers was reduced to less than $\sim 1.65\%$ and $\sim 0.65\%$ of the original sky levels in B - and R -bands, respectively.

Finally, we generated the combined mosaic images with FoV of $\sim 3^\circ \times 3^\circ$ in B - and R -bands. We found that a local spatial fluctuation exists in the vicinity of the target galaxy, inducing the uncertainty in sky determination. Although the variation of the sky level due to the sky fluctuation was less than $\sim 0.05\%$ of the original sky brightness, it introduced an additional and dominant uncertainty in the surface brightness profile. Taking this effect into account, we derived the surface brightness profiles of NGC 1291. As a result, we were able to reach the surface brightness of $\mu_{B,1\sigma} \sim 29.5$ and $\mu_{R,1\sigma} \sim 28.5$ mag arcsec $^{-2}$ in one-dimensional light profiles, respectively. It suggested that the deep images obtained with KMTNet are suitable to detect the tidal debris, outer disks and dwarf galaxies (Martínez-Delgado et al. 2010), but might not be ideal to analyze faint diffuse stellar halos (Johnston et al. 2008; Courteau et al. 2011; Bakos & Trujillo 2012). As we discussed above, the achieved imaging depth is mainly limited by the local fluctuation of the sky value rather than the integration time or large-scale sky variation. Therefore, our observing strategy is well optimized to achieve our scientific goal. Based on the result of this study, we decided to focus on

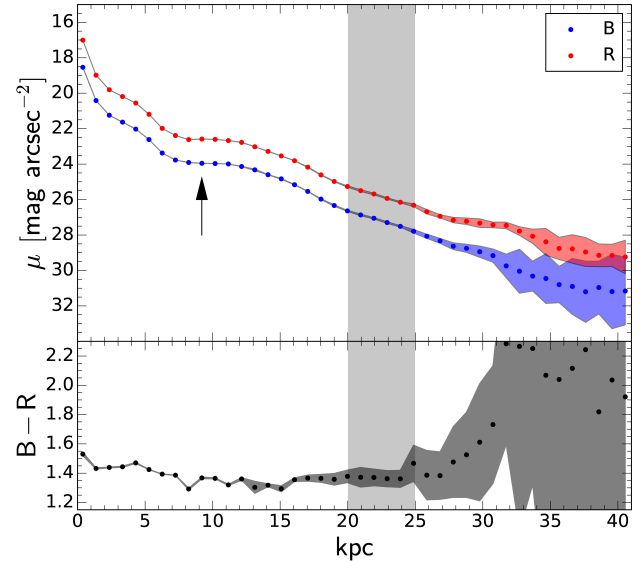


Figure 10. *Top:* The surface brightness profiles of NGC 1291. The galaxy outskirts appear to be detected up to ~ 34 kpc with a $1\text{-}\sigma$ depth of $\sim 28.5\text{--}29.5$ mag arcsec $^{-2}$. The error budget (lightly shaded region) is estimated to be the quadratic sum of the variance in the isophote and the scatter of the profiles induced by the uncertainty in sky determination. The position of the outer ring is indicated by an arrow. The vertically shaded area represents the inner radius where the stellar halos are expected to dominate the stellar light (see the text for details). *Bottom:* $B-R$ color profile. It appears to have a nearly flat gradient up to ~ 25 kpc.

exploring outer disks in XUV-disk galaxies, and dwarf companions in nearby late-type galaxies, which are thought to be brighter than our depth limit. In addition, we will also obtain I -band and $H\alpha$ imaging data for better understandings of the stellar populations and current star formation in the outskirts. We are planning to expand sample size and investigate photometric characteristics of the outskirts of individual target galaxies including extended disk profiles and dwarf companions in upcoming papers.

We are grateful to an anonymous referee for constructive comments and suggestions. We thank Zhao-Yu Li and Hua Gao for useful discussion. This research has made use of the KMTNet system operated by the Korea Astronomy and Space Science Institute (KASI) and the data were obtained at three host sites of CTIO in Chile, SAAO in South Africa, and SSO in Australia. This research was supported by the Basic Science Research Program through the National Research Foundation of Korea (NRF) funded by the Ministry of Science, ICT & Future Planning (No. NRF-2017R1C1B2002879). L.C.H. was supported by the National Key R&D Program of China (2016YFA0400702) and the National Science Foundation of China (11473002, 11721303).

REFERENCES

- Atkinson, A. M., Abragam, R. G., & Ferguson, A. M. N. 2013, *ApJ*, 765, 28
 Bakos, J., Trujillo, I., & Pohlen, M. 2008, *ApJL*, 683, 103
 Bakos, J., & Trujillo, I. 2012, arXiv:1204.3082
 Bertin, E., & Arnouts, S. 1996, *A&AS*, 117, 393
 Bertin, E., Mellier, Y., Radovich, M. et al. 2002, *ASPC*, 281, 228
 Bertin, E. 2006, *ASPC*, 351, 112
 Bovy, J., & Rix, H.-W. 2013, *ApJ*, 779, 115
 Bullock, J. S., Kravtsov, A. V., & Weinberg, D. H. 2001, *ApJ*, 548, 33
 Bullock, J. S., & Johnston, K. V. 2005, *ApJ*, 635, 931
 Carollo, D., Beers, T. C., Chiba, M. et al. 2010, *ApJ*, 712, 692
 Cooper, A. P., Cole, S., Frenk, C. S. et al. 2010, *MNRAS*, 406, 744

- Courteau, S., Widrow, L. M., McDonald, M. et al. 2011, *ApJ*, 739, 20
- De Lucia, G., & Helmi, A. 2008, *MNRAS*, 391, 14
- Duc, P.-A., Cuillandre, J.-C. Karabal, E. et al. 2015, *MNRAS*, 446, 120
- de Vaucouleurs, G. 1975, *ApJS*, 29, 193
- Feldmeier, J. J., Ciardullo, R., Jacoby, G. H., & Durrell P. R. 2004, *ApJ*, 615, 196
- Harmsen, B., Monachesi, A., Bell, E. F. et al. 2017, *MNRAS*, 466, 1491
- Hinz, J. L., Engelbracht, C. W., Skibba, R. et al. 2012, *ApJ*, 756, 75
- Ho, L. C., Li, Z.-Y., Barth, A. J., Seigar, M. S., Peng, C. Y. 2011, *ApJS*, 197, 21
- Johnston, K. V., Bullock, J. S., Sharma, S. et al. 2008, *ApJ*, 689, 936
- Kim, S.-L., Lee, C.-U., Park, B.-G. et al. 2016, *JKAS*, 49, 37
- Li, J.-T., Wang, Q. D., Li, Z., & Chen, Y. 2011, *ApJ*, 737, 41
- Lupton, R. H. 2005, in *SDSS Data Release 14, Transformations between SDSS Magnitudes and other systems*, www.sdss.org/dr14/algorithms/sdssUBVRITransform#Lupton2005
- Malin, D. F. 1979, *Natur*, 277, 279
- Martínez-Delgado, D. Gabany, R. J., Crawford, K. et al. 2010, *AJ*, 140, 962
- Merritt, A., van Dokkum, P., Abraham, R., Zhang, J. 2016, *ApJ*, 830, 62
- Mihos, J. C., Harding, P., Spengler, C. E., Rudick, C. S., Feldmeier, J. J. 2013, *ApJ*, 762, 82
- Mihos, J. C., Harding, P., Feldmeier, J. J. et al. 2017, *ApJ*, 834, 16
- Morales, G., Martínez-Delgado, D., Grebel, E. K. et al. 2018, arXiv:1804.03330
- Park, H. S., Moon, D.-S., Zaritsky, D. et al. 2017, *ApJ*, 848, 19
- Pillepich, A., Vogelsberger, M. Deason, A. et al. 2014, *MNRAS*, 444, 237
- Pohlen, M., & Trujillo, I. 2006, *A&A*, 454, 759
- Radburn-Smith, D. J., de Jong, R. S., Seth, A. C. et al. 2011, *ApJS*, 195, 18
- Schweizer, F. 1980, *ApJ*, 237, 303
- Schweizer, F., Seitzer, P. 1988, *ApJ*, 328, 88
- Sheen, Y.-K., Yi, S. K., Ree, C. H., & Lee, J. 2012, *ApJS*, 202, 8
- Tal, T., van Dokkum, P. G., Nelan, J., & Bezanson, R. 2009, *ApJ*, 183, 1417
- Thilker, D. A., Bianchi, L., Meurer, G. et al. 2007, *ApJS*, 173, 538
- Trujillo, I., & Fliri, J. 2016, *ApJ*, 823, 123
- van den Bergh, S. 2010, *AJ*, 140, 1043
- van Dokkum, P. G. 2005, *AJ*, 130, 2647
- van Dokkum, P. G., Abraham, R., & Merritt, A. 2014, *ApJL*, 782, 24
- van Vledder, I., van der Vlugt, D., Holwerda, B. W. et al. 2016, *MNRAS*, 458, 425
- Watkins, A. E., Mihos, J. C., & Harding, P. 2015, *ApJL*, 800, 3
- Watkins, A. E., Mihos, J. C., & Harding, P. 2016, *ApJ*, 826, 59
- White, S. D. M., Rees, M. J. 1978, *MNRAS*, 183, 341